Int. J. Solids Structures Vol. 29, No. 13, pp. 1613–1636, 1992
Printed in Great Britain.

0020–7683/92 $5.00+ .00

INDENTATION OF POROUS SOLIDS

N. A. FLECK
Engineering Department, Cambridge University, Cambridge, CB2 1PZ, U.K.

H. OTOYO
Department of Mechanical Engineering, Science University of Tokyo, Noda-Shi, Chiba-Ken 278, Japan

and

A. NEEDLEMAN
Division of Engineering, Brown University, Providence, RI 02912, U.S.A.

(*Received* 18 *July* 1991; *in revised form* 8 *October* 1991)

Abstract—The effect of porosity upon indentation resistance is explored for a sticking conical indenter. Two material models are used: the Gurson model which is appropriate for lower porosities, where there are well separated voids that are roughly spherical in shape, and the particle yield model of Fleck *et al.* (1992) *J. Mech. Phys. Solids* which is appropriate for a microstructure consisting of spherical particles joined by discrete necks. Finite strain finite element calculations and a cavity expansion model both show that the indentation pressure is 2–3 times the uniaxial yield strength of the porous solid, for initial porosities of up to 0.3. Compaction occurs in a plastic zone of roughly hemispherical shape surrounding the indenter. Full density is achieved along the flanks of the indenter for initial porosities of less than 0.1, but not for higher porosities. Both the finite element and cavity expansion models suggest that the average indentation pressure increases as the cone is made sharper (smaller included angle at the apex of the cone), as the yield strain of the material decreases and as the level of initial porosity decreases. For comparison purposes, finite element results are presented for fully dense solids. The predictions of the finite element analysis for a porous solid are also compared with the experimental results for indentation of a sintered steel. Very good agreement is found for both the indentation load and for the deformation field.

1. INTRODUCTION

Sintered metals, ceramics and polymers are finding increased engineering use due to the advantages which they offer in terms of processing and mechanical properties. Near net final shaped components can be manufactured from metallic powders ranging from steels to rapidly solidified aluminum–lithium alloys. Structural ceramics such as silicon carbide and silicon nitride, and polymers such as PTFE are made by hot pressing. A characteristic feature of sintered materials is their porosity, which ranges from 0 to 0.5. In tribological applications such as gears and bearings, the porosity may be used to advantage by impregnating the material with a liquid or solid lubricant, such as oils and graphite.

A potential problem in the use of sintered materials is their resistance to indentation and wear. It is observed experimentally that the indentation pressure using a Vickers pyramidal indenter is approximately equal to three times the uniaxial yield strength of a sintered material. Whilst it is commonly accepted that the indentation pressure of fully dense metals is three times their yield strength, it is not clear why this ratio is preserved for porous solids. In the limit of extremely high porosites >0.5 materials are cellular in nature; then, the indentation pressure is approximately equal to the uniaxial yield strength of the material (Wilsea *et al.*, 1975). Gibson and Ashby (1988) interpret the results of Wilsea *et al.* (1975) for cellular solids in terms of the low value of the "plastic Poisson's ratio" for a cellular solid: under uniaxial compression there is a small degree of transverse plastic straining. In an indentation test there is little development of plastic constraint, thus the indentation pressure for a cellular solid is approximately equal to the uniaxial compressive yield strength. We shall show in the present paper that for sintered materials the shape of the yield surface is such that, in an indentation test, some build up of plastic constraint occurs and the indentation pressure exceeds the uniaxial yield strength.

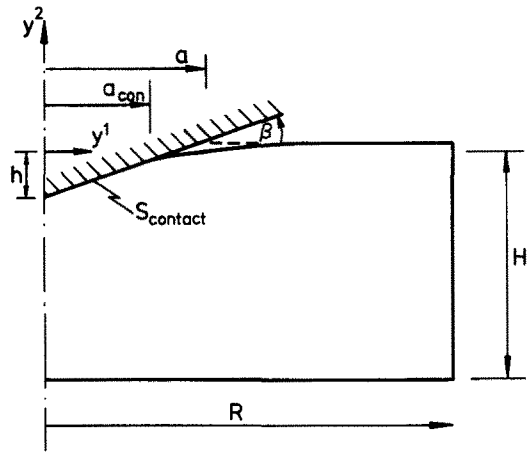

Fig. 1. Geometry of the boundary value problem; h is the depth of indentation, a_{con} is the actual contact radius and $a = h/\tan\beta$ defines a nominal contact radius.

In the present study, the effect of porosity upon conical indentation is explored using a finite element analysis. The boundary value problem analyzed is sketched in Fig. 1 and two porous plastic constitutive relations are considered: the Gurson (1977) solid, and a more recent particle model of highly porous solids by Fleck *et al.* (1992), which will be referred to as the FKM model. The Gurson constitutive relation is appropriate at lower porosities, where there are well separated voids that are roughly spherical in shape. The FKM model is more appropriate at larger porosities, where the microstructure consists of spherical particles joined by discrete necks and is applicable up to porosities of 0.36, which is the limit of dense random packing of spherical particles.

For both constitutive relations indentation is approximated by a cavity expansion model, which is an extension of the model of Johnson (1970) to plastically compressible solids. The cavity expansion model is qualitatively accurate in showing the effect of porosity, elastic modulus and indenter angle upon the indentation pressure. Experimental results are presented for the indentation resistance of a sintered steel. The indentation pressure and deformation field predicted by the finite element analysis compare favorably with the corresponding observations.

2. CONSTITUTIVE RELATIONS

Two constitutive descriptions are used to model the effect of porosity upon indentation response: a modified version of the Gurson constitutive relation (Gurson, 1975) and a modified version of the particle yielding relation of Fleck *et al.* (1992).

As in continuum damage mechanics, see e.g. Lemaitre (1985), we account for the dependence of the elastic properties on porosity. For both material models we assume that the elastic modulus E and Poisson's ratio ν scale linearly with porosity f, and vanish in the limit of dense random packing of the sintered powder $f = \hat{f} = 0.36$. Hence,

$$E = E_0(\hat{f} - f)/\hat{f}, \quad \nu = \nu_0(\hat{f} - f)/\hat{f} \tag{1}$$

where E_0 and ν_0 are Young's modulus and Poisson's ratio of the matrix material, respectively. The relations (1) approximately fit the experimental data summarized by Rice (1977).

The rate of deformation tensor $\mathbf{d} = \dot{F} \cdot F^{-1}$, with F being the deformation gradient and a superposed dot denoting the time derivative, is written as the sum of an elastic part, $\mathbf{d}^e$, and a plastic part, $\mathbf{d}^p$, so that

$$\mathbf{d} = \mathbf{d}^{\mathrm{e}} + \mathbf{d}^{\mathrm{p}}. \tag{2}$$

Elastic strains are assumed to remain small and the elastic constitutive response is represented approximately by the hypoelastic relation

$$\hat{\boldsymbol{\sigma}} = L : \mathbf{d}^{\mathrm{e}} \tag{3}$$

where

$$L = \frac{E}{1+\nu}\left[\mathrm{I}' + \frac{\nu}{1-2\nu}\,\mathrm{II}\right] \tag{4}$$

with $\hat{\boldsymbol{\sigma}}$ being the Jaumann rate of Cauchy (true) stress, I the second order indentity tensor and I′ the fourth order identity tensor.

The plastic part, $\mathbf{d}^{\mathrm{p}}$, is obtained from the flow rule, which for the constitutive relations used is of the form,

$$\mathbf{d}^{\mathrm{p}} = \dot{\Lambda}\frac{\partial \Phi}{\partial \boldsymbol{\sigma}}. \tag{5}$$

Combining (2), (3) and (5) gives

$$\hat{\boldsymbol{\sigma}} = L : \mathbf{d} - \dot{\Lambda} L : \frac{\partial \Phi}{\partial \boldsymbol{\sigma}}. \tag{6}$$

2.1. *Gurson solid*

Based on an approximate analysis of the yielding of a thick spherical shell made from rigid, perfectly-plastic material Gurson (1977) suggested a yield condition of the form

$$\Phi(\boldsymbol{\sigma}, \bar{\sigma}, f) = \frac{\sigma_{\mathrm{e}}^2}{\bar{\sigma}^2} + 2q_1 f \cosh\left(\frac{3q_2\sigma_h}{2\bar{\sigma}}\right) - 1 - q_1^2 f^2 = 0. \tag{7}$$

Here,

$$\sigma_{\mathrm{e}}^2 = \tfrac{3}{2}\boldsymbol{\sigma}' : \boldsymbol{\sigma}', \quad \sigma_h = \tfrac{1}{3}\boldsymbol{\sigma} : \mathrm{I}, \quad \boldsymbol{\sigma}' = \boldsymbol{\sigma} - \sigma_h \mathrm{I} \tag{8}$$

and $\bar{\sigma}$ and f are the matrix flow strength and void volume fraction, respectively. The parameters q_1 and q_2 were introduced by Tvergaard (1981); based on the cell model studies of Koplik and Needleman (1988), we take $q_1 = 1.25$ and $q_2 = 1$.

By setting the plastic work rate equal to the matrix dissipation rate, the plastic flow proportionality factor, $\dot{\Lambda}$, in (5) is found to be

$$\dot{\Lambda} = \frac{(1-f)\bar{\sigma}\dot{\bar{\varepsilon}}}{\boldsymbol{\sigma} : \dfrac{\partial \Phi}{\partial \boldsymbol{\sigma}}}. \tag{9}$$

The flow potential (7) contains two internal variables, the porosity f and the average matrix flow strength, $\bar{\sigma}$. An initial porosity, f_0, is specified and the rate of change of void volume fraction is determined from the condition that the matrix material is plastically incompressible,

$$\dot{f} = (1-f)\mathbf{d}^{\mathrm{p}} : \mathrm{I}. \tag{10}$$

Attention here is focussed on the rate-independent, elastic–perfectly-plastic matrix material response for which $\bar{\sigma}$ is constant. However, the finite element calculations are based on a

formulation for rate dependent and strain hardening material behavior. Specifically, the matrix plastic strain rate is given by

$$\dot{\bar{\varepsilon}} = \dot{\varepsilon}_0 \left(\frac{\bar{\sigma}}{g(\bar{\varepsilon})} \right)^{1/m}. \tag{11}$$

Here $\dot{\varepsilon}_0$ and m are constants and

$$g(\bar{\varepsilon}) = \sigma_0 [1 + \bar{\varepsilon}/\varepsilon_0]^N, \quad \varepsilon_0 = \frac{\sigma_0}{E} \tag{12}$$

where σ_0 is a reference strength.

In order to simulate a nearly rate independent, perfectly-plastic response, we take $m = 0.01$, $N = 0.001$ and the imposed loading rates are adjusted so that the strain rates do not vary enough from $\dot{\varepsilon}_0$ to significantly affect stress levels. In the following σ_0 is referred to as the matrix yield strength.

2.2. *FKM solid*

Fleck *et al.* (1992) have recently developed a yield surface for an isotropic aggregate of spherical particles which are bonded together at isolated necks. The model assumes that the circular necks between particles yield plastically in the manner found by Green (1954) for the plane strain yielding of a junction between two half-planes. The macroscopic yield surface was calculated on the assumption that there is no interaction between neighboring necks. Fleck *et al.* (1992) found that the yield surface is quadratic in shape and is given by

$$\Phi(\boldsymbol{\sigma}, \bar{\sigma}, f) = \left(\frac{5}{18} \frac{\sigma_e}{p_y} + 2 \right)^2 + \left(\frac{\sqrt{5}}{3} \frac{\sigma_h}{p_y} \right)^2 - 1 = 0 \tag{13}$$

where the yield strength under hydrostatic loading, p_y, is

$$p_y = \frac{2.97}{\hat{f}} (1 - f)^2 (\hat{f} - f) \bar{\sigma} \tag{14}$$

and $\hat{f} = 0.36$ is the porosity for dense random packing of undeformed spheres.

As for the Gurson solid, the proportionality factor $\dot{\Lambda}$ is determined by setting the macroscopic plastic work rate equal to the matrix dissipation rate, see Fleck *et al.* (1992), giving

$$\dot{\Lambda} = \frac{5.35(1 - f)^2 (\hat{f} - f)^{3/2} \bar{\sigma} \dot{\bar{\varepsilon}}}{\boldsymbol{\sigma} : \dfrac{\partial \Phi}{\partial \boldsymbol{\sigma}}}. \tag{15}$$

The internal variables appearing in (13) are f and $\bar{\sigma}$ as for the Gurson solid. The evolution equation for f is given by (10) and a rate-independent, perfectly-plastic matrix material response is simulated as described in the previous section. In the FKM relation, an important role is played by the combination of f and $\bar{\sigma}$, defined in (14), and denoted by p_y. The expression in (14) arises from treating each particle contact as an isolated neck. In the early stages of plastic deformation, the necks joining each particle are small in size and few in number, and the assumption of isolated neck response is reasonable. As f decreases, the necks increase in area and the number of necks per particle increase. Here, (14) is modified to account for the reduction in plastic constraint associated with the necks ceasing to act in an isolated manner.

According to Helle *et al.* (1985), the number of necks per particle z, increases as

$$z = 12(1-f). \tag{16}$$

Now, consider a linear array of three particles, each of radius R_0, such that they are joined by circular necks of radius x. The neck radius is given by the average value for an aggregate of porosity f (Helle *et al.*, 1985)

$$\frac{x}{R_0} = \left(\frac{\hat{f}-f}{3\hat{f}}\right)^{1/2}. \tag{17}$$

Imagine that the three particles are pressed together along their line of centers. When the neck radius x is small ($x \ll R_0$) the average pressure p at each neck is approximately that given by the Prandtl punch solution, $[(2+\pi)/\sqrt{3}]\bar{\sigma} \approx 2.97\bar{\sigma}$. As x/R_0 increases p drops due to overlap of the plastic zones emanating from each neck. An estimate of the average indentation pressure is achieved from the plane strain forging solution of a bar between two frictionless opposing punches. We identify the bar thickness as $2R_0$ and the width of each punch as $2x$. Hill (1950) gives the average indentation pressure as a function of R_0/x. His graphical results are closely fitted by the piecewise-linear relation,

$$p = \begin{cases} (2+\pi)k, & \dfrac{R_0}{x} \geqslant 7.5; \\ 2k + \dfrac{\pi}{6.5}\left(\dfrac{R_0}{x} - 1\right)k, & 1 < \dfrac{R_0}{x} < 7.5; \\ 2k, & \dfrac{R_0}{x} \leqslant 1. \end{cases} \tag{18}$$

The relations (17) and (18) are used to modify p_y, and hence the yield surface (13), by redefining p_y as,

$$p_y = \frac{2.97}{\hat{f}} F_1(f)(1-f)^2(\hat{f}-f)\bar{\sigma} \tag{19}$$

where

$$F_1(f) = \begin{cases} 1 & f \geqslant 0.34; \\ \dfrac{1}{2+\pi}\left[2 + \dfrac{\pi}{6.5}\left(\left[\dfrac{3\hat{f}}{\hat{f}-f}\right]^{1/2} - 1\right)\right] & f < 0.34. \end{cases} \tag{20}$$

The yield surface (13) with (19) and (20) gives rise to a vertex on the hydrostatic stress axis in (σ_e, σ_h) space. This vertex is a consequence of the vertex in the Green (1954) plane strain slip line field solution for yielding at a junction between two half-planes. Tabor (1959) and Calladine (1971) argue that such a vertex does not actually exist for a circular neck. In any case, we note that the vertex on the FKM yield surface differs from the sort of vertex that arises in metal crystal plasticity. The FKM vertex is at a fixed location on the yield surface, namely $\sigma_e = 0$, whereas the loading point for a metal crystal is generally at a vertex. Here, for numerical reasons, we round off the vertex by a quadratic approximation to the yield surface near to the vertex. We write,

$$\frac{\sigma_e}{p_y} = A\left(c - \left|\frac{\sigma_h}{p_y}\right|\right)^{1/2} \tag{21}$$

as the approximation to the yield surface near to the vertex, and select constants A and c such that the yield surface (21) is continuous in value and in slope with the more general

description (13) at $|\sigma_h| = 0.970p_y$. The quadratic approximation (21) gives hydrostatic straining under hydrostatic stressing, and thereby eliminates the vertex on the yield surface.

We use (13) in conjunction with (19) and (20) to represent the yield surface for an aggregate of particles joined by necks. This FKM yield surface is compared with corresponding yield surfaces of the Gurson (1975) model in Fig. 2.

Predictions of the FKM model under proportional axisymmetric loading are given in Fig. 3. Consider first uniaxial compression. For an elastic–perfectly-plastic matrix, the porous solid shows strong geometric hardening due to neck growth as shown in Fig. 3a. The stress versus strain curves are concave in shape. The effect of matrix hardening on the uniaxial compression response is shown in Fig. 3b; the increase in strength due to matrix strain hardening at any given strain level exceeds that due to compaction for $N > 0.1$. For the case shown of $f_0 = 0.3$, strain hardening causes the stress–strain curves to have a convex shape at low strains; with further straining the strong geometric hardening causes the curves to be concave.

Now consider uniaxial compression with a superimposed radial stress proportional to the axial stress. As an illustration we take the case of an elastic–perfectly-plastic matrix and $f = 0.3$. An increasing hydrostatic component of stress leads to more rapid compaction and to stronger geometric hardening, see Fig. 4.

3. CAVITY EXPANSION MODEL

Marsh (1964) and Johnson (1970) have idealized the process of conical indentation by the elastic–perfectly-plastic expansion of a spherical cavity. The indentation process is idealized by encasing the indenter in a rigid hemispherical "core" of material of radius a, under a hydrostatic pressure equal to the mean indentation pressure $\bar{p}$, see Fig. 5a. As sketched in this figure, the cavity expansion model presumes that neither pile-up- nor sink-in occur so that a_{con}/a in Fig. 1 is unity. Full field solutions to be presented subsequently show that this is a very good approximation for porous solids. Outside the core, it is assumed that the stress and displacement fields have radial symmetry, and are the same as for an infinite, incompressible, elastic–perfectly-plastic body which contains a void of radius a under pressure $\bar{p}$. Material within the elastic–plastic boundary at a radius $c > a$ is in a plastic state; material outside the elastic–plastic boundary behaves elastically. Johnson (1970) argues that at the boundary of the core stresses are continuous, and the radial displacement of material points during an increment of penetration must accommodate the volume of material displaced by the indenter. At the outer elastic–plastic boundary $r = c$,

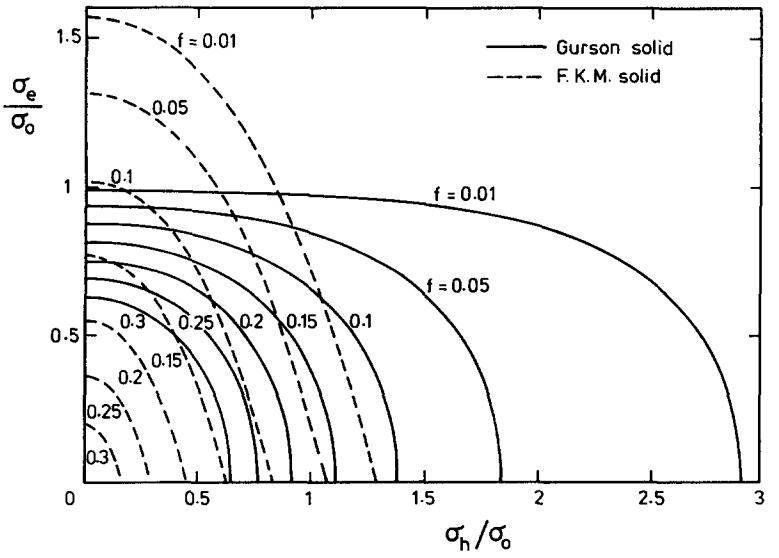

Fig. 2. Comparison of yield surfaces for the Gurson solid and the FKM solid.

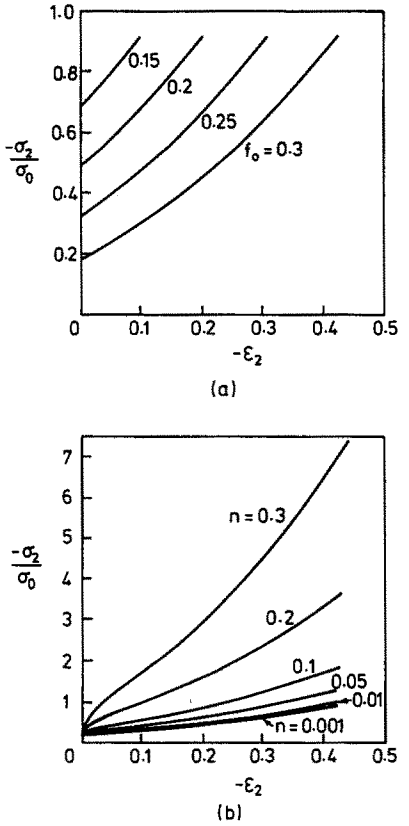

Fig. 3. True stress versus logarithmic strain response of FKM solid under uniaxial compression. $E_0/\sigma_0 = 1000$, $\nu_0 = 0.3$. (a) Effect of porosity for an elastic–perfectly-plastic matrix. (b) Effect of strain hardening with initial porosity $f_0 = 0.3$.

displacements and stresses are continuous. These assumptions are sufficient to solve the problem analytically to give

$$\frac{\bar{p}}{Y} = \frac{2}{3}\left[1 + \ln\left(\frac{1}{3}\frac{E}{Y}\tan\beta\right)\right] \tag{22}$$

where Y is the uniaxial yield strength of the material. Equation (22) shows that the indentation pressure $\bar{p}$ is a function predominantly of the non-dimensional group $E\tan\beta/Y$. We may interpret this group as the ratio of the representative strain beneath the indenter $\tan\beta$ to the yield strain Y/E of the indented material. Johnson (1970) showed that this elastic–perfectly-plastic model gives good agreement with the observed indentation pressure for a variety of materials and cone angles provided $2 < E\tan\beta/Y < 30$. At $E\tan\beta/Y < 2$ indentation is almost entirely elastic, while for $E\tan\beta/Y > 30$ elasticity no longer plays any role and material displaced by the indenter piles up at the sides in the manner suggested by rigid–perfectly-plastic theory.

Johnson (1970) used the cavity expansion model to demonstrate the effect of elasticity upon the indentation pressure $\bar{p}$. Here, we use the model to show the effect of a uniform initial porosity f_0 upon $\bar{p}$. We assume that the core region $r < a$ is rigid and suffers a uniform hydrostatic stress state, see Fig. 5a. Material in the hemispherical shell $a < r < c$ suffers elastic–plastic straining and undergoes compaction ($\dot{f} < 0$), while material beyond the elastic–plastic boundary strains elastically.

We consider the rate problem where the indenter descends at a constant velocity $\dot{h}$, causing material to displace radially at a velocity $v(r)$. A steady state indentation pressure $\bar{p}$ is achieved whereby $\bar{p}$ and c/a do not change with time. We use the equilibrium, compatibility and stress–strain relations for the elastic–plastic body in order to determine a set

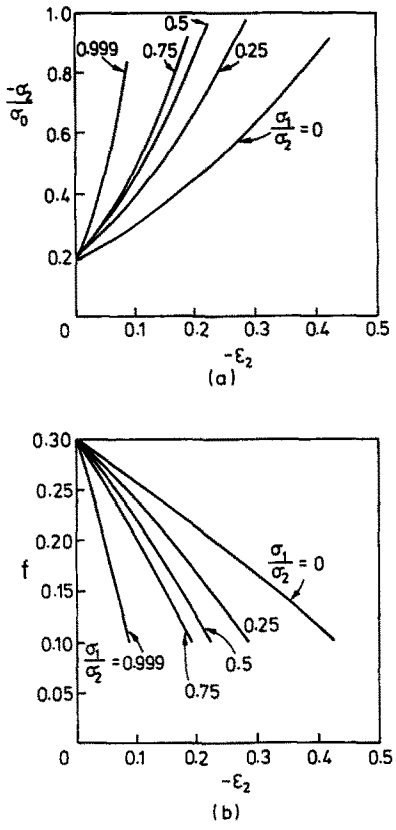

Fig. 4. Response of the FKM solid with initial porosity $f_0 = 0.3$ to proportional multi-axial compression. $E_0/\sigma_0 = 1000$, $\nu_0 = 0.3$. (a) True stress versus logarithmic strain. (b) Evolution of porosity.

of four first order differential equations in the variables σ_r, σ_θ, v and f. Matching the velocity at $r = a$ and $r = c$ is sufficient to determine c/a and thence $\bar{p}$.

The constitutive description of the material is taken either to be the FKM solid or the Gurson solid. At time t, the core surrounding the indenter is of radius a and a representative material element, initially at radius r_0, has displaced radially by a distance u to a radius $r = r_0 + u$. Self-similarity of the solution dictates that the Cauchy stress $\boldsymbol{\sigma}$ and porosity f are functions only of the non-dimensional radius $\xi = r/a$. The radius of the hydrostatic core a serves as a natural measure of time. The radial displacement of a material element $u(r, a)$ may be written $u = ag(\xi)$ where $g(\xi)$ is an unknown function of ξ.

First, we consider the strain–displacement relations for a material element in the deformed configuration in terms of spherical polar coordinates (r, θ, ϕ) and associated unit base vectors $(\mathbf{e}_r, \mathbf{e}_\theta, \mathbf{e}_\phi)$, defined in Fig. 5a. A material point has an instantaneous velocity v, where

$$\mathbf{v} = v(\xi)\mathbf{e}_r \tag{23}$$

giving rise to active components of the rate of deformation tensor,

$$d_r = \frac{\partial v}{\partial r} = \frac{\mathrm{d}v}{a\,\mathrm{d}\xi}, \quad d_\theta = d_\phi = \frac{v}{r} = \frac{1}{a}\frac{v}{\xi}. \tag{24}$$

Equilibrium dictates that

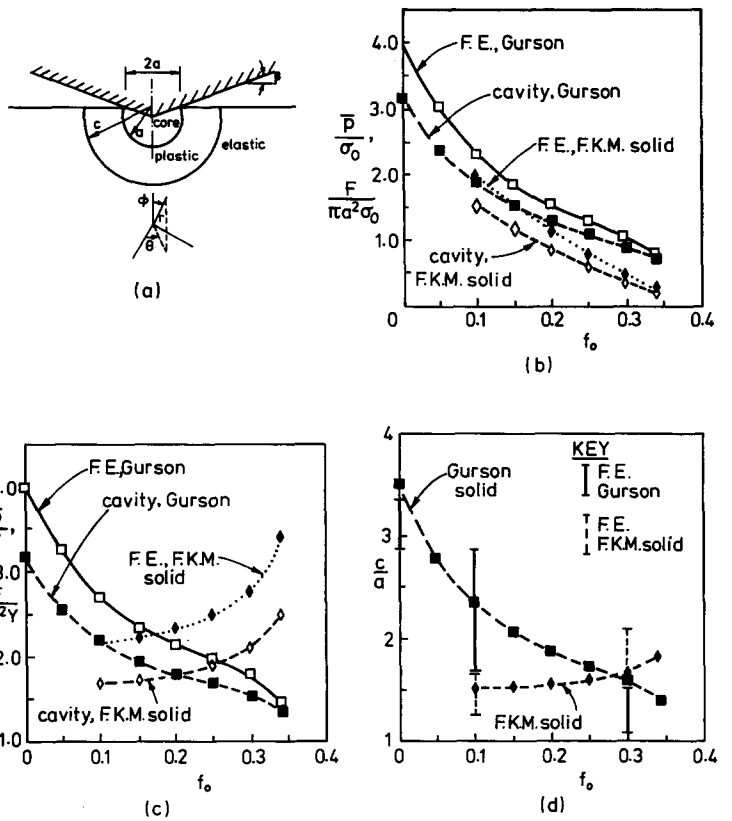

Fig. 5. Comparison of predictions of the cavity expansion model with the finite element calculations. $E_0/\sigma_0 = 500$, $\nu_0 = 0.3$, $\beta = 19.7°$. (a) Geometry of the cavity expansion model. (b) Indentation pressure normalized by the matrix strength $\bar{\sigma}$ versus porosity f_0. (c) Indentation pressure normalized by the aggregate uniaxial yield strength Y versus porosity f_0. (d) Radius of plastic zone c normalized by contact semi-width a versus f_0. The finite element results predict that the plastic zone extends deeper into the solid than it does laterally. The error bars display the range of plastic zone radius with angular co-ordinate from the finite element analysis.

$$\frac{\partial \sigma_r}{\partial \xi} = \frac{2(\sigma_\theta - \sigma_r)}{\xi} \tag{25}$$

where the symmetry condition $\sigma_\theta = \sigma_\phi$ has been exploited.

The rate of change of porosity $\dot{f}$ of a material point is assumed to be dependent on the volumetric part of the plastic strain rate through (10). The rate of change of porosity at a fixed material point is given by

$$\dot{f} = \frac{\mathrm{d}f}{\mathrm{d}\xi}\left(\frac{v}{a} - \frac{\xi \dot{a}}{a}\right). \tag{26}$$

Similarly, the rate of change of each stress component at a fixed material point is

$$\dot{\sigma}_i = \frac{\mathrm{d}\sigma_i}{\mathrm{d}\xi}\left(\frac{v}{a} - \frac{\xi \dot{a}}{a}\right), \quad i = r, \theta, \phi. \tag{27}$$

Using the evolution equations (10), (24) and (27) in (26) gives

$$\frac{\mathrm{d}f}{\mathrm{d}\xi}\left(\frac{v}{a}-\frac{\xi\dot{a}}{a}\right)=(1-f)\left[\frac{2}{a}\frac{v}{\xi}+\frac{1}{a}\frac{\mathrm{d}v}{\mathrm{d}\xi}-\frac{1-2\nu}{E}\left(\frac{\mathrm{d}\sigma_r}{\mathrm{d}\xi}+2\frac{\mathrm{d}\sigma_\theta}{\mathrm{d}\xi}\right)\left(\frac{v}{a}-\frac{\xi\dot{a}}{a}\right)\right]. \tag{28}$$

Similarly, (25) gives

$$\frac{\mathrm{d}\sigma_r}{\mathrm{d}\xi}\left(\frac{v}{a}-\frac{\xi\dot{a}}{a}\right)=L_{rr}\frac{1}{a}\frac{\mathrm{d}v}{\mathrm{d}\xi}+2L_{r\theta}\frac{1}{a}\frac{v}{\xi} \tag{29}$$

$$\frac{\mathrm{d}\sigma_\theta}{\mathrm{d}\xi}\left(\frac{v}{a}-\frac{\xi\dot{a}}{a}\right)=L_{\theta r}\frac{1}{a}\frac{\mathrm{d}v}{\mathrm{d}\xi}+(L_{\theta\theta}+L_{\theta\phi})d_\theta \tag{30}$$

where

$$\dot{\sigma}_i=L_{ij}d_j,\quad i=r,\phi,\theta. \tag{31}$$

Explicit expressions for the elastic–plastic tangent moduli L are given in Fleck *et al.* (1992).

Material in the core $r\leqslant a$ is taken to be rigid and under hydrostatic pressure $\bar{p}$. Incompressibility of the core material dictates

$$2\pi a^2 v=\pi a^2\dot{h}\quad\text{at}\quad r=a \tag{32}$$

where the indentation rate $\dot{h}=\dot{a}\tan\beta$ by geometry. Thus, the radial velocity at the edge of the core, at $\xi=1$, is

$$v(1)=\frac{\dot{a}}{2}\tan\beta. \tag{33}$$

The outer boundary condition is obtained by matching the stress and velocity to the Lamé solution for a pressurized elastic sphere, see Hill (1950) and Timoshenko and Goodier (1970). With c denoting the radius of the elastic–plastic boundary, which must be determined by the analysis, and with $\xi_c=c/a$

$$v(\xi_c)=\tfrac{3}{2}\xi_c\left(\frac{E}{B(1+\nu)}+1\right)^{-1}\dot{a} \tag{34}$$

where $B=2\sigma_e(\xi_c)/3$.

Equations (25) and (28) through (31) constitute a system of four first order non-linear ordinary differential equations for σ_r, σ_θ, v and f. We integrate these relations and iterate with an assumed value of $\xi_c=c/a$ until the velocity condition (33) is satisfied at the inner boundary $\xi=1$, and (34) is satisfied at the outer boundary $\xi=\xi_c$. Integration of the system of equations is by a Runge–Kutta scheme.

3.1. *Predictions*

The effect of porosity upon the indentation pressure predicted by the cavity expansion model is given in Figs 5b, c. Throughout this paper unless otherwise stated, β is taken as 19.7° in order to give the same displaced volume as the Vickers pyramid. Also, we set $E_0/\sigma_0=500$ and $\nu_0=0.3$. We note that the indentation pressure normalized by the marix yield strength σ_0 decreases with increasing initial porosity f_0 for both the Gurson and the FKM solids, see Fig. 5b. When the indentation pressure is normalized by the uniaxial yield strength of the porous aggregate Y, the effect of increasing the porosity is to decrease the normalized pressure for the Gurson solid but increase the normalized pressure for the FKM solid.

The cavity expansion model for both the Gurson and FKM solids shows that the compaction zone around the indenter is more localized in extent than for the fully dense

solid, see Fig. 5d. For f_0 in the range $0.10 < f_0 < 0.35$, the cavity expansion model gives $c/a = 1.5-2.5$ for both constitutive laws.

Plastic compaction leads to geometric hardening and to diffuse plastic straining within the plastic zone around the indenter. A typical plot of the stresses and porosity within the compaction zone is displayed in Fig. 6a for the Gurson solid with initial porosity $f_0 = 0.1$. With decreasing distance from the indenter, the porosity decreases to a value of 0.040 at $r = a$, while the absolute magnitude of the radial stress component increases. Both the hoop stress and the hydrostatic change sign within the compaction zone, and become compressive near the indenter. The absolute magnitude of $\dot{f}$ and of the matrix plastic strain rate $\dot{\bar{\varepsilon}}$ are greatest near the indenter, as shown in Fig. 6b. Straining of material elements is axisymmetric with a variable hydrostatic stress within the plastic zone.

Results for the FKM solid with initial porosity $f_0 = 0.3$ are given in Figs 6c, d. The cavity expansion model predicts that the porosity decreases to a value of 0.227 at $r = a$. The hoop stress is close to zero within the plastic zone, and the indentation load is carried mostly by the radial stresses. The compaction rate is highest immediately adjacent to the indenter.

The cavity expansion model suggests that the indentation pressure $\bar{p}$ may be written in the non-dimensional form,

$$\frac{\bar{p}}{\sigma_0} = \mathscr{F}\left(\frac{E}{\sigma_0}, \tan\beta, f, \nu\right) \tag{35}$$

where σ_0 is the matrix flow strength, see (1), and ν plays little role. In the incompressible

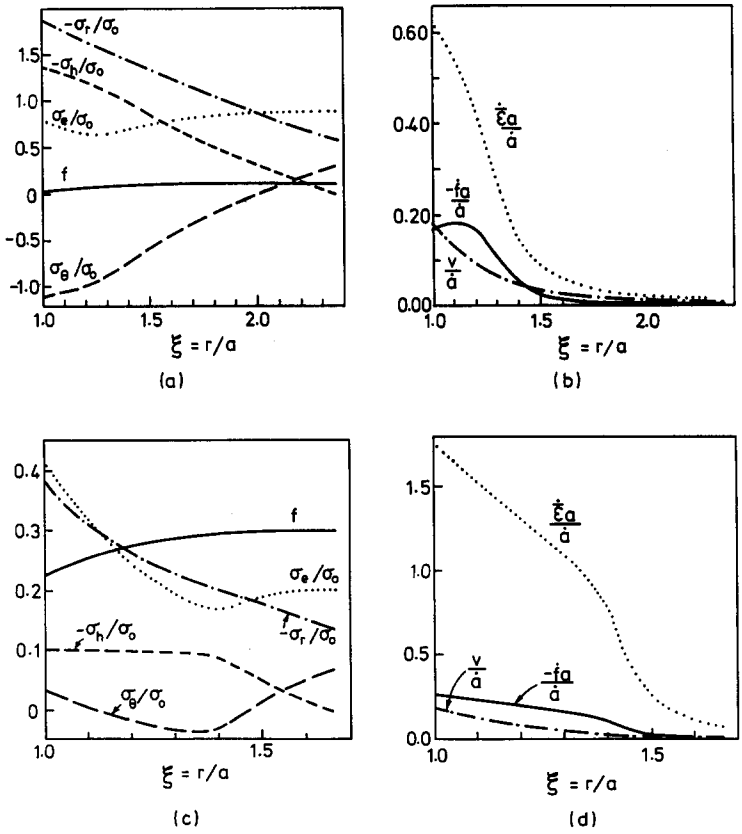

Fig. 6. Predictions of the cavity expansion model. $E_0/\sigma_0 = 500$, $\nu_0 = 0.3$, $\beta = 19.7°$. Spatial dependence of (a) stresses and porosity, and (b) rate quantities for the Gurson solid, with initial porosity $f_0 = 0.1$. Spatial dependence of (c) stresses and porosity, and (d) rate quantities for the FKM solid, with initial porosity $f_0 = 0.3$.

limit of $f = 0$ and $\nu = 0.5$, the cavity expansion model reduces to that given by Johnson (1970), and (22) is recovered.

The effect of indenter angle β and elastic modulus E_0 on the average indentation pressure is shown in Fig. 7. The cavity model exhibits the same qualitative trends as the finite element results: $\bar{p}$ increases with increasing β and with increasing E_0/σ_0. The effect of elastic modulus on indentation pressure decreases with increasing porosity. The cavity model assumes that the pressure required to expand a spherical cavity in an infinite elastic–plastic solid is approximately equal to the indentation pressure. Hill (1950) has shown that a cavitation state exists such that continued expansion of the cavity occurs at a limiting finite pressure. Elastic deformation in the far field is required in order for the cavitation pressure to be finite. In the limit of a rigid–perfectly-plastic porous solid the cavitation pressure is unbounded.

4. NUMERICAL METHOD AND RESULTS

The numerical method is based on a convected coordinate Lagrangian formulation of the field equations, with the initial unstressed state taken as reference. This formulation has been employed extensively in previous finite element analyses and is reviewed in Needleman (1982). All field quantities are taken to be functions of convected coordinates, y^i, which serve as particle labels, and time t. With attention confined to quasi-static deformations and with body forces neglected, the rate form of the principle of virtual work is

$$\Delta t \int_V [\dot{\tau}^{ij}\delta E_{ij} + \tau^{ij}\dot{u}^k_{,i}\delta u_{k,j}]\,\mathrm{d}V = \Delta t \int_S \dot{T}^i \delta u_i\,\mathrm{d}S - \left[\int_V \tau^{ij}\delta E_{ij}\,\mathrm{d}V - \int_S T^i \delta u_i\,\mathrm{d}S\right]. \quad (36)$$

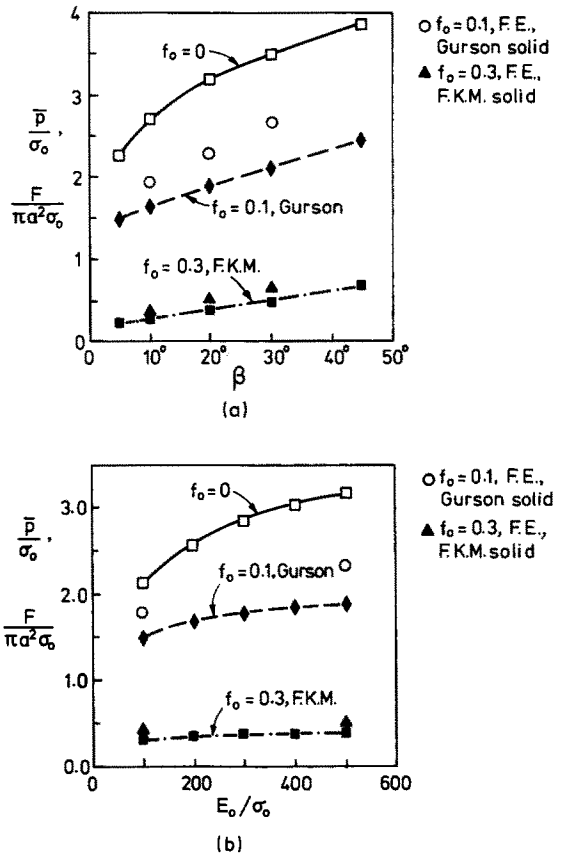

Fig. 7. Effect of (a) indenter angle and (b) Young's modulus upon the average indentation pressure predicted by the cavity model. Predictions from the finite element analysis are included. In (a) $E_0/\sigma_0 = 500$, in (b) $\beta = 19.7°$. $\nu_0 = 0.3$ throughout.

Here, V and S are the volume and surface, respectively, of the body in the reference configuration and $(\dot{}) = \partial(\ )/\partial t$ at fixed y^i. The contravariant components of the Kirchhoff stress, τ^{ij}, are given by $\tau^{ij} = J\sigma^{ij}$, where J is the ratio of current to reference volume of a material element and σ^{ij} are the contravariant components of the Cauchy (or true) stress on the deformed convected coordinate net. The second term on the right-hand side is an equilibrium correction term that reduces drift from the equilibrium path due to the discrete time step in the numerical procedure.

The nominal traction components, T^i, and the Lagrangian strain components, E_{ij}, are given by

$$T^i = (\tau^{ij} + \tau^{kj} u^i_{,k}) v_j \tag{37}$$

$$E_{ij} = \tfrac{1}{2}(u_{i,j} + u_{j,i} + u^k_{,i} u_{k,j}) \tag{38}$$

where u_j are the components of the displacement vector on base vectors in the reference configuration, $(\ )_{,i}$ denotes covariant differentiation in the reference frame and v is the surface normal in the reference configuration.

A cylindrical coordinate system (r, θ, z) is used and the identifications $y^1 = r$, $y^2 = z$ and $y^3 = \theta$ are made. Attention is confined to axisymmetric deformations so that all field quantities are independent of θ. The problem analysed is the indentation of a circular cylindrical block of a porous plastic solid of uniform initial porosity f_0 by a rigid conical punch, see Fig. 1. At the current stage of deformation, the depth of indentation is denoted by h and the contact radius by a_{con}. In general, due to pile-up or sink-in a_{con} differs from the nominal contact radius, $a = h/\tan\beta$, and is determined as part of the solution to the rate boundary value problem. Perfect sticking is assumed as soon as the block comes into contact with the punch, so that the rate boundary conditions are

$$\dot{u}_1 = 0, \quad \dot{u}_2 = -\dot{h} \quad \text{on} \quad S_{\text{contact}} \tag{39}$$

where S_{contact} denotes the portion of the block surface in contact with the punch. The other boundary conditions are

$$\dot{u}_2 = 0, \quad \dot{T}^1 = 0 \quad \text{on} \quad y^2 = -H \tag{40}$$

$$\dot{u}_1 = 0, \quad \dot{T}^2 = 0 \quad \text{on} \quad y^1 = 0 \tag{41}$$

and $\dot{T}^1 = \dot{T}^2 = 0$ on the remaining external surface.

Most of the results presented are based on a finite element mesh consisting of a 29×29 array of quadrilateral elements, as shown in Fig. 8. Each quadrilateral element is made up of four linear displacement crossed triangular elements. The aim in the numerical calculations is to simulate indentation of a semi-infinite block. The only relevant length for the semi-infinite block boundary value problem is a (or h). To simulate this situation numerically, attention is confined to a regime where h, a and the plastic zone size are small compared to the block dimensions H and R, see Fig. 1. The discretization also introduces another characteristic length into the problem, the mesh size. In the calculations with the 29×29 quadrilateral mesh, each quadrilateral side in the fine uniform mesh shown in Fig. 8b is of length 0.2 in arbitrary units. In these same arbitrary units $H = R = 40$. Standard kinematic identities are used to transform the stress rate–strain rate relation (6) into one involving the stress rate and strain rate measures appearing in (36). The deformation history is calculated in a linear incremental manner. In order to increase the stable time step, the rate tangent modulus method of Peirce *et al.* (1984) is used.

4.1. *Fully dense solids*

For comparison purposes, solutions were obtained for fully dense solids. Numerically, these were obtained using the Gurson flow potential, (7), with the initial porosity, f_0, taken to be zero. Figure 9 shows semi-log plots of the computed values of $F/(\pi a^2 \sigma_0)$, $F/(\pi a_{con}^2 \sigma_0)$ and a_{con}/a, against $\tan\beta/\varepsilon_0$. The points shown in this figure were computed using

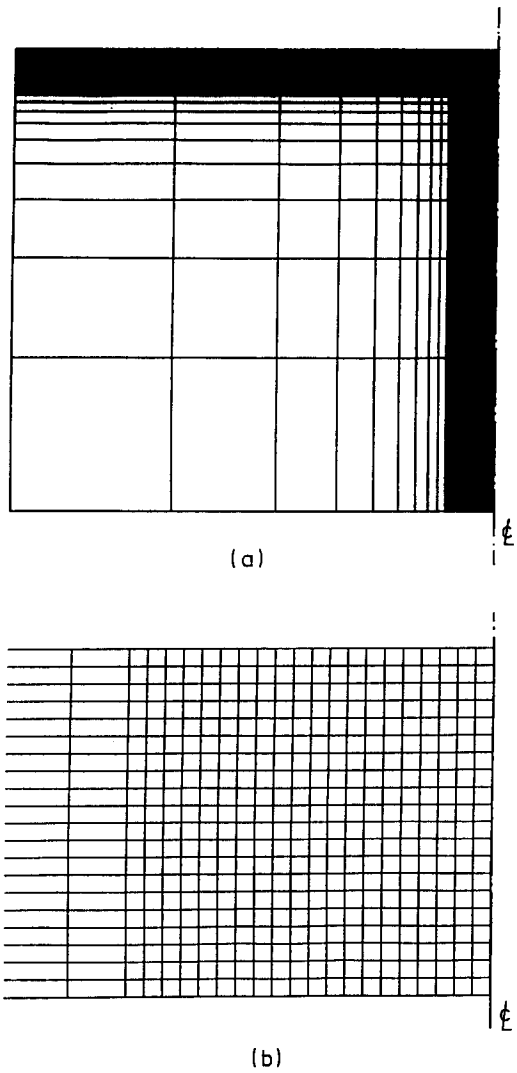

Fig. 8. Finite element mesh used for most of the calculations. (a) The complete mesh, (b) refined mesh local to the region of indentation.

values of $E/\sigma_0 = 1/\varepsilon_0$ ranging from 28.8 to 700 and values of β between 2.5° and 30°. There appears to be a plateau in the nominal contact pressure, with $F/(\pi a^2\sigma_0) \approx 4$ for $\tan\beta/\varepsilon_0$ between 180 and 300. The plateau in actual contact pressure, $F/(\pi a_{con}^2\sigma_0) \approx 3$ occurs for $\tan\beta/\varepsilon_0 > 35$. The point at $\tan\beta/\varepsilon_0 = 11.6$ was obtained using $E/\sigma_0 = 28.8$ and $\beta = 22°$, which corresponds to values used by Bhattacharya and Nix (1988) in their finite element calculation of indentation of Si ($\nu = 0.278$ in this calculation, whereas $\nu = 0.3$ in all of our other calculations). In Fig. 9, $F/(\pi a_{con}^2\sigma_0) = 2.23$, whereas Bhattacharya and Nix (1988, Fig. 11) obtain $F/(\pi a_{con}^2\sigma_0) = 2.4$ for a frictionless cone. Also shown in Fig. 9a are lines representing a linear least square fit to the nominal contact pressure, $F/(\pi a^2\sigma_0)$, over their extent. The linear fit is quite good in each of these extents. The regime $\tan\beta/\varepsilon_0 < 35$ corresponds to the range where sink-in occurs, $a_{con}/a < 1$. As seen in Fig. 9b, for $35 < \tan\beta/\varepsilon_0 < 179$, pile-up occurs and a_{con}/a is an increasing function of $\tan\beta/\varepsilon_0$. The amount of pile-up appears to saturate for $\tan\beta/\varepsilon_0 > 179$.

The predictions of the cavity expansion model are compared with the finite element results for the fully dense solid in Fig. 9. In the cavity expansion regime, say $30 < (E\tan\beta)/\sigma_0 < 100$, the cavity expansion model consistently underpredicts the indentation pressure by $2\sigma_0/3$. Johnson (1985) accounts for this discrepancy by arguing that the material in the core region immediately beneth the indenter is not under a hydrostatic stress

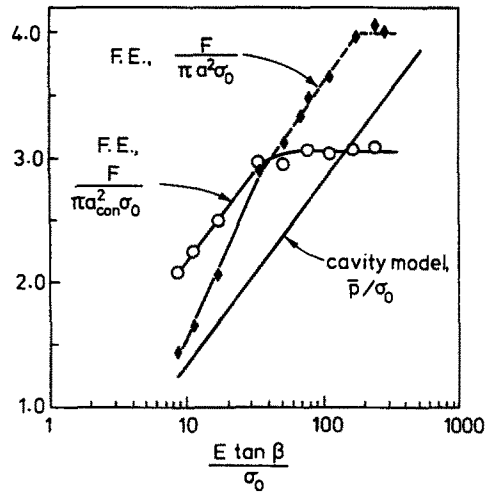

(a)

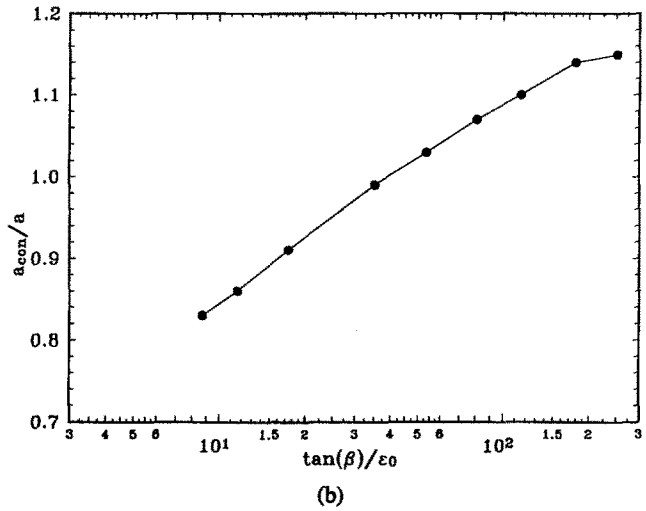

(b)

Fig. 9. (a) Normalized indentation pressures for the fully dense, elastic–perfectly plastic solid. (b) Ratio of true contact radius, a_{con}, to nominal contact radius $a = h/\tan \beta$, where h is the depth of indentation, for the fully dense, elastic–perfectly plastic solid. $\nu_0 = 0.3$.

state. He assumes a cylindrical stress state, such that the material is at yield and $\bar{p}$ denotes the hydrostatic component of stress. The normal stress along the indentation direction is $-(\bar{p}+2\sigma_0/3)$ and the radial stress is $-(\bar{p}-\sigma_0/3)$. This pragmatic modification to the cavity expansion model brings its predictions into better agreement with the finite element results for the nominal contact pressure, $F/(\pi a^2 \sigma_0)$. We have not used this modification as its interpretation is not straightforward for the porous solid; for the porous solid the yield strength in the core region beneath the indenter is sensitive to the local levels of pressure and porosity.

Figure 10a shows the effect of the discretization on the computed response. The mesh spacing in the uniform region of the finer meshes is half that of the 29×29 quadrilateral mesh. As can be seen in this figure, the force oscillates due to successive contact of surface nodes by the punch. The amplitude of the force oscillation is quite high initially, but by the time several nodes have come into a contact with the punch, the oscillation amplitude has decreased substantially. After $a \approx 0.4$ in Fig. 10a, which corresponds to two contact nodes for the 29×29 mesh, the force amplitudes obtained from the two meshes coincide. Figure

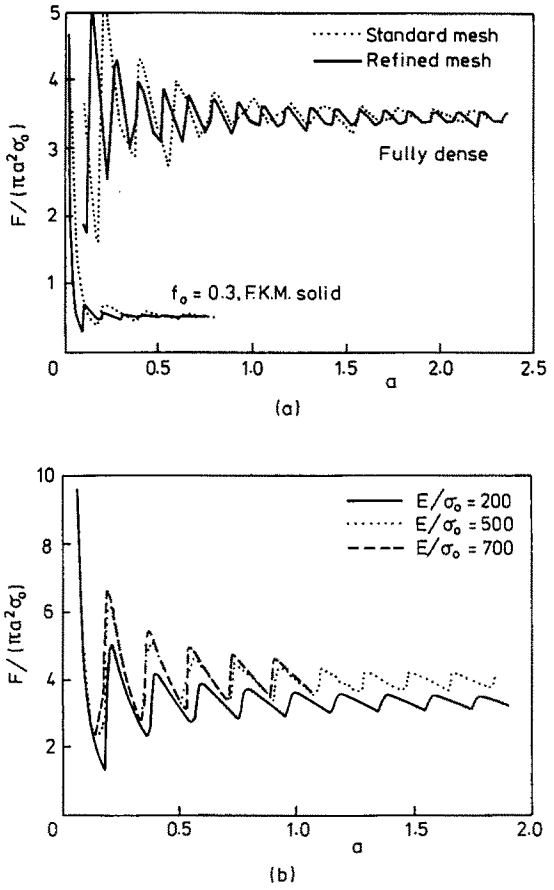

Fig. 10. (a) Effect of mesh refinement upon average indentation pressure, (b) effect of yield strain upon average indentation pressure. $\nu_0 = 0.3$, $\beta = 19.7°$, $E/\sigma_0 = 200$ unless otherwise stated.

10a also shows a convergence study using the FKM constitutive relation for a porous solid having an initial porosity $f_0 = 0.3$. In this case, the force amplitude oscillations are smaller and decrease more rapidly with increasing a than for the fully dense case. Because of the variation of E with f embodied in (1), the porous aggregate has a larger value of ε_0 than does the fully dense solid. In general, the oscillation amplitude decreases with increasing ε_0. For a given calculation, the value of indentation pressure reported in Fig. 9 and in subsequent figures is the average of the last peak value and the minimum value preceding that peak. In order to check the effect of the crude outer mesh on the computed response, the fully dense calculation with $\tan\beta/\varepsilon_0 = 71.6$ was repeated using a 42×42 quadrilateral mesh. This mesh had the same resolution in the uniform region as did the 29×29 quadrilateral mesh in Fig. 8, with the increase in resolution going into the outer mesh. The computed nominal contact pressure, $F/(\pi a^2\sigma_0)$, was 3.34 as compared with 3.32 using the 29×29 quadrilateral mesh. The comparison of our results with those of Bhattacharya and Nix (1988), together with the convergence studies in Fig. 10, indicates that mesh induced stiffness is not responsible for the numerically obtained plateaus for $F/(\pi a^2\sigma_0)$ and a_{con}/a.

The variation of average contact pressure with E/σ_0, keeping all other parameters at fixed values, is shown in Fig. 10b. The nominal contact pressure $F/(\pi a^2\sigma_0)$, initially increases with E/σ_0 and then eventually appears to approach an asymptotic value, which in Fig. 10b is ≈ 4, for $\beta = 19.7°$.

Figure 11 shows deformed meshes near the punch for $\beta = 15°$, $E/\sigma_0 = 200$, giving $\tan\beta/\varepsilon_0 = 53.6$ and for $\beta = 19.7°$, $E/\sigma_0 = 500$, giving $\tan\beta/\varepsilon_0 = 179$. With $\tan\beta/\varepsilon_0 = 179$, there is a considerably increased shear of mesh lines as they approach the punch surface as compared to the case where $\tan\beta/\varepsilon_0 = 53.6$. The increased pile-up associated with high values of $\tan\beta/\varepsilon_0$ can also be seen in this figure.

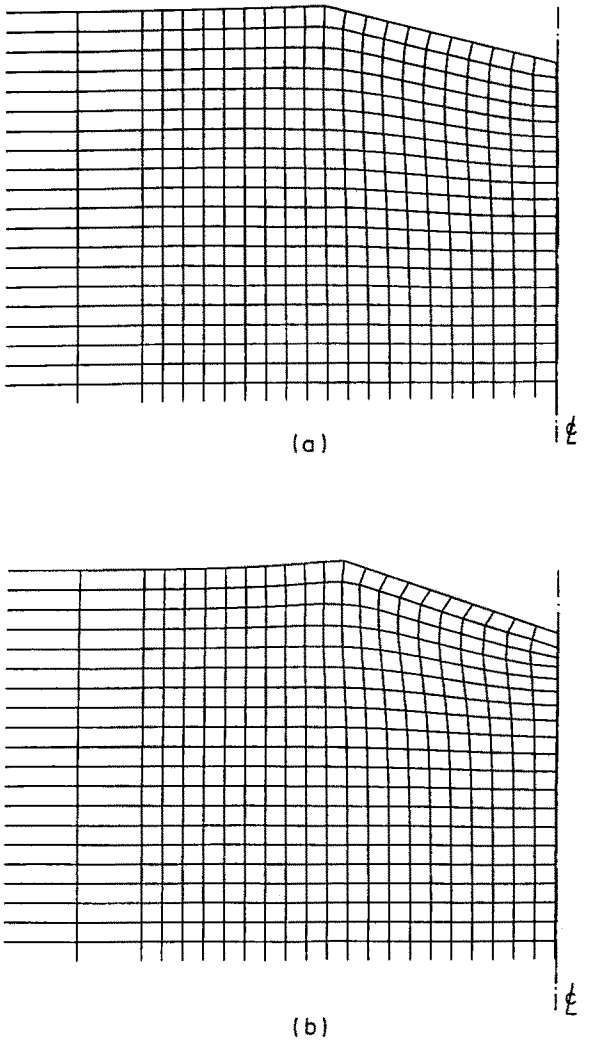

Fig. 11. Deformed mesh for fully dense solid. (a) $\tan \beta/\varepsilon_0 = 53.6$, (b) $\tan \beta/\varepsilon_0 = 179$.

4.2. *Porous solids*

The computed nominal indentation pressures are shown in Fig. 5, where they are compared with the corresponding predictions based on the cavity expansion model for $\beta = 19.7°$, $E_0/\sigma_0 = 500$ and $\nu = 0.3$. As mentioned in Section 3, the cavity expansion model assumes $a_{con}/a \approx 1$. The finite element computations show that this is a very good approximation for porous solids. For example, for the case of Gurson solid with $f_0 = 0.05$, $a_{con}/a = 1.05$, which can be compared with $a_{con}/a = 1.14$ for the corresponding fully dense solid. For both the FKM and Gurson solids with $0.1 \leqslant f_0 \leqslant 0.3$, a_{con}/a was found to lie between 0.95 and 1.0.

It is clear that the cavity expansion model gives the same qualitative trends as the finite element results. The predicted pressures are 20–30% less than the finite element values; this is not surprising as cavity expansion is an easier deformation mode and involves almost proportional loading. The cavity model gives a prediction of the extent of the plastic zone which is in good agreement with the finite element predictions, see Fig. 5d. Both the cavity expansion model and the finite element analysis predict that the ratio c/a increases with increasing f for the FKM solid, but decreases with increasing f for the Gurson solid. For the fully dense solid, the cavity expansion model overpredicts the extent of the plastic zone.

Experimental measurement of indentation pressure for sintered metals show that $F/(\pi a_{con}^2 Y)$ lies in the range 2.5–3.5 for $0.05 < f_0 < 0.35$ (Talmage, 1961; Salak *et al.*, 1974).

Presuming that the Gurson solid is appropriate for a porosity f_0 of less than 0.15, while the FKM solid is more relevant at higher porosities, the finite element results in Fig. 5c suggest that the predicted values of normalized indentation pressure, $F/(\pi a_{con}^2 Y)$, are within the range of experimental scatter.

Figures 12–15 show contour plots of various field quantities in the vicinity of the punch tip for four cases; (a) a Gurson solid with $f_0 = 0.1$, (b) an FKM solid with $f_0 = 0.1$, (c) a Gurson solid with $f_0 = 0.3$ and (d) an FKM solid with $f_0 = 0.3$. In each case $\beta = 19.7°$. The stage of deformation shown in each case corresponds to the same depth of indentation. The deformed profiles in these figures show the lack of pile-up or sink-in for porous solids.

As seen in Fig. 12, the two constitutive relations give very similar contours of matrix plastic strain, $\bar{\varepsilon}$, when $f_0 = 0.1$, but when $f_0 = 0.3$, much more extensive straining is predicted by the FKM constitutive relation. By way of contrast, Fig. 13 shows that lower hydrostatic stress magnitudes are predicted by the FKM relation at both initial porosities. Even though the matrix plastic strain distributions for the Gurson and FKM solids are very similar when $f_0 = 0.1$, Fig. 14 shows that a much larger highly compacted zone is predicted by the FKM constitutive relation in this case. When $f_0 = 0.3$, Figs 14c, d, the shape of the porosity contours are very similar to the shape of the corresponding matrix plastic strain contours in Figs 12c, d and reflect the more extensive compaction region predicted for the FKM solid. Contours of constant porosity rate, $\dot{f}$, are shown in Fig. 15. For both $f_0 = 0.1$ and $f_0 = 0.3$, the Gurson constitutive relation predicts higher porosity rates within a narrower region.

Although contours of field quantities for the fully dense solid are not shown here, we note that a main effect of porosity is to lower the hydrostatic stress level; for example, for a fully dense solid and for both $\tan\beta/\varepsilon_0 = 53.6$ and $\tan\beta/\varepsilon_0 = 179$, the hydrostatic stress

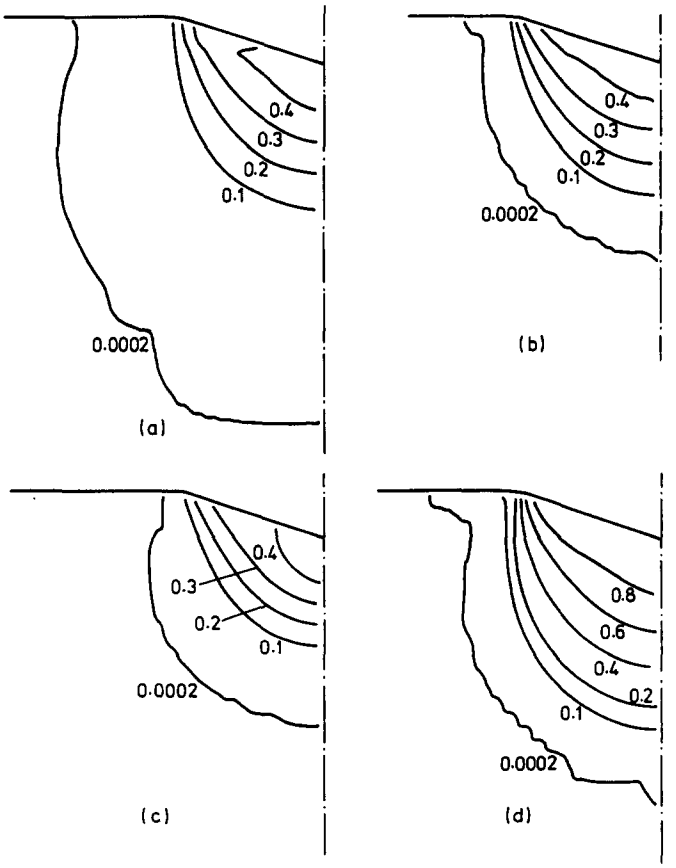

Fig. 12. Contours of constant matrix plastic strain $\bar{\varepsilon}$ for (a) Gurson solid, with initial porosity $f_0 = 0.1$, (b) FKM solid, with initial porosity $f_0 = 0.1$, (c) Gurson solid, with initial porosity $f_0 = 0.3$, (d) FKM solid, with initial porosity $f_0 = 0.3$. $E_0/\sigma_0 = 500$, $\nu_0 = 0.3$, $\beta = 19.7°$.

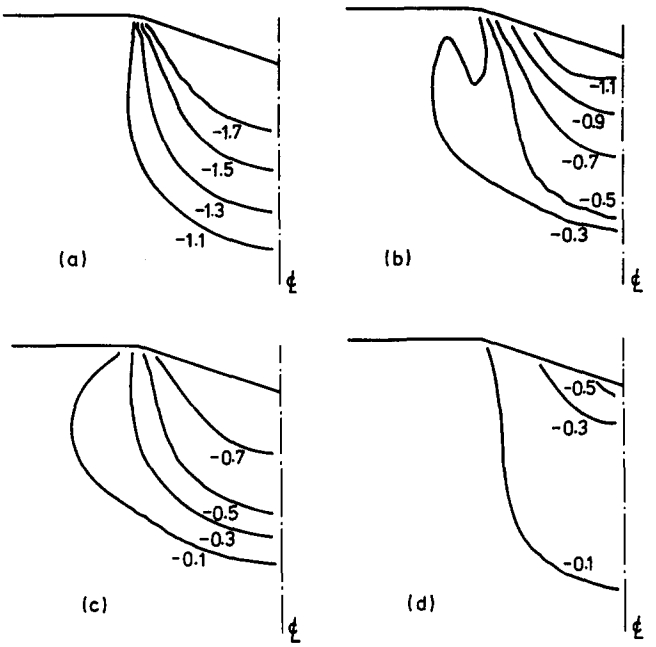

Fig. 13. Contours of constant normalized hydrostatic stress, σ_h/σ_0, for (a) Gurson solid, with initial porosity $f_0 = 0.1$, (b) FKM solid, with initial porosity $f_0 = 0.1$, (c) Gurson solid, with initial porosity $f_0 = 0.3$, (d) FKM solid, with initial porosity $f_0 = 0.3$. $E_0/\sigma_0 = 500$, $\nu_0 = 0.3$, $\beta = 19.7°$.

level at the depth of the $-1.7\sigma_0$ contour in Fig. 13a is about $-2.3\sigma_0$. Also, for the fully dense solid the plastic strain contours are not as circular as those in Fig. 12a and become more ellipsoidal with increasing values of $\tan\beta/\varepsilon_0$. With $\tan\beta/\varepsilon_0 = 179$, the ratio of the major axis, which lies parallel to the free surface, to the minor axis, which lies along the center line, is 1.2:1.

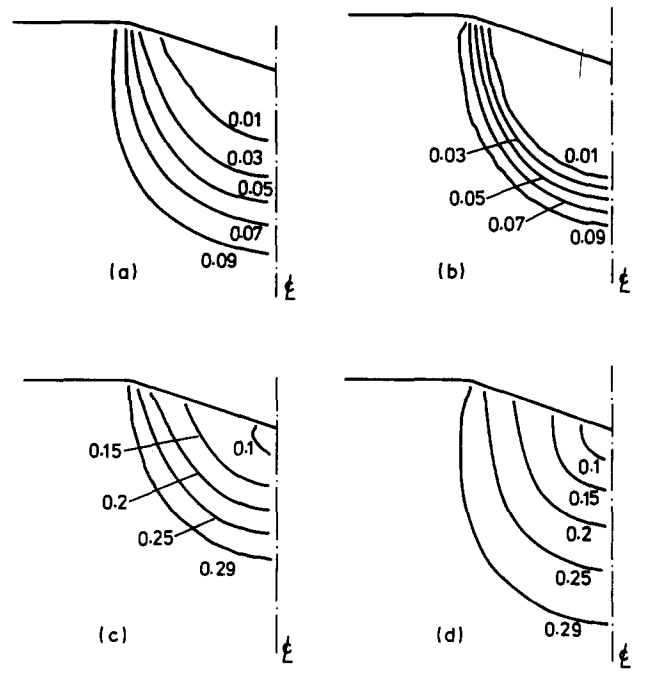

Fig. 14. Contours of constant porosity, f, for (a) Gurson solid, with initial porosity $f_0 = 0.1$, (b) FKM solid, with initial porosity $f_0 = 0.1$, (c) Gurson solid, with initial porosity $f_0 = 0.3$, (d) FKM solid, with initial porosity $f_0 = 0.3$. $E_0/\sigma_0 = 500$, $\nu_0 = 0.3$, $\beta = 19.7°$.

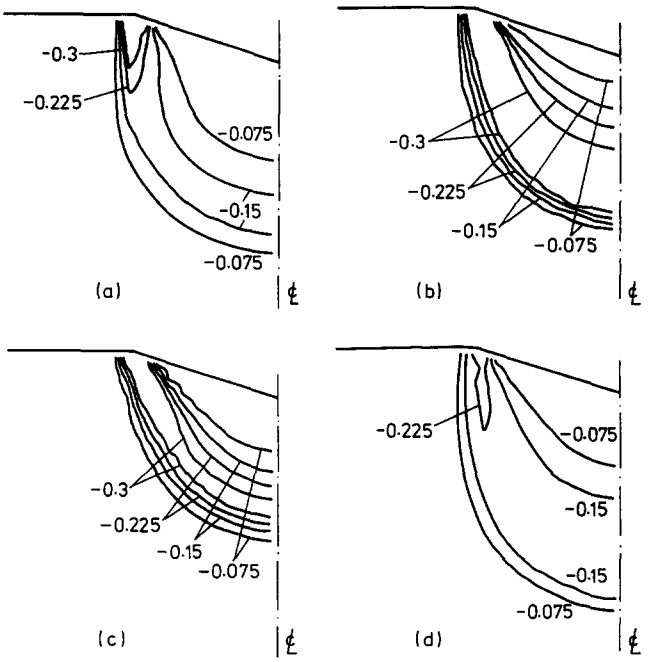

Fig. 15. Contours of constant porosity rate, $\dot{f}h/\dot{H}$, for (a) Gurson solid, with initial porosity $f_0 = 0.1$, (b) FKM solid, with initial porosity $f_0 = 0.1$, (c) Gurson solid, with initial porosity $f_0 = 0.3$, (d) FKM solid, with initial porosity $f_0 = 0.3$. $E_0/\sigma_0 = 500$, $\nu_0 = 0.3$, $\beta = 19.7°$.

Figure 16 shows variations in field quantities under the punch tip. Here, x measures the current distance from the punch tip and is normalized by the contact length a. The values shown are the average values in the quadrilateral element along $y^1 = 0$. Each of the plots in Fig. 16 contains points from at least three stages of indentation. The fact that points from the various stages of indentation give a common curve illustrates that self-similarity is attained in the finite element solutions. In Fig. 16a, where $f_0 = 0.1$ and the calculation uses the Gurson constitutive relation, the magnitudes of both the hydrostatic stress and the macroscopic effective stress attain a maximum close to the indenter. Also, the material directly under the punch is essentially fully compacted. In Fig. 16b, which pertains to $f_0 = 0.3$ and the FKM constitutive relation, the hydrostatic and effective stress magnitudes attain their maximum at the punch tip (in this case the value of σ_e/σ_0 in the single quadrilateral element directly under the punch is ≈ 1.02; this high value is due to accumulated time stepping errors). Also, the material in the first element under the punch has a residual porosity of about 0.05.

A comparison of Figs 6 and 16 shows that the spatial distributions of stress and porosity predicted by the cavity expansion model are qualitatively similar to those obtained from the finite element analyses. However, the finite element results show a greater degree of compaction and higher hydrostatic stresses underneath the indenter than predicted by the cavity expansion model. For the Gurson solid with an initial porosity of 0.1, the finite element analysis predicts that full compaction to zero porosity occurs beneath the indenter. The cavity model suggests that compaction is not complete and that $f = 0.040$ adjacent to the indenter. For the FKM solid, with an initial porosity of 0.3, the cavity expansion model predicts $f = 0.227$ adjacent to the indenter, while the finite element results give $f = 0.05$. For the Gurson solid with $f_0 = 0.1$ and for the FKM solid with $f_0 = 0.3$, the cavity expansion model and the finite element results predict that significant compaction begins at a distance approximately $1.5a$ ahead of the indenter.

5. COMPARISON WITH EXPERIMENTS

An indentation test was performed on 0.1% carbon sintered steel, in order to compare with the predictions of the finite element analysis. Sintered steel bars were used of porosity

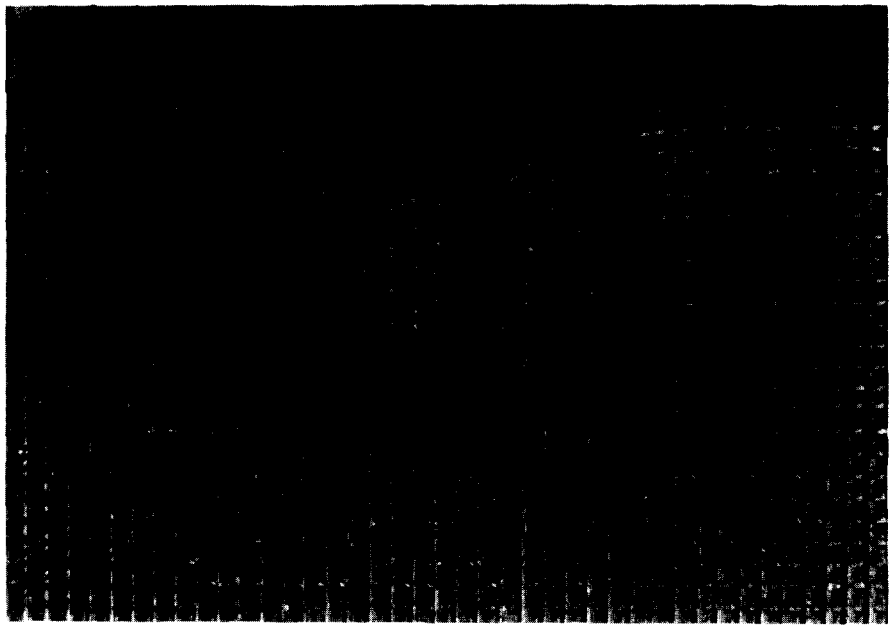

(a)

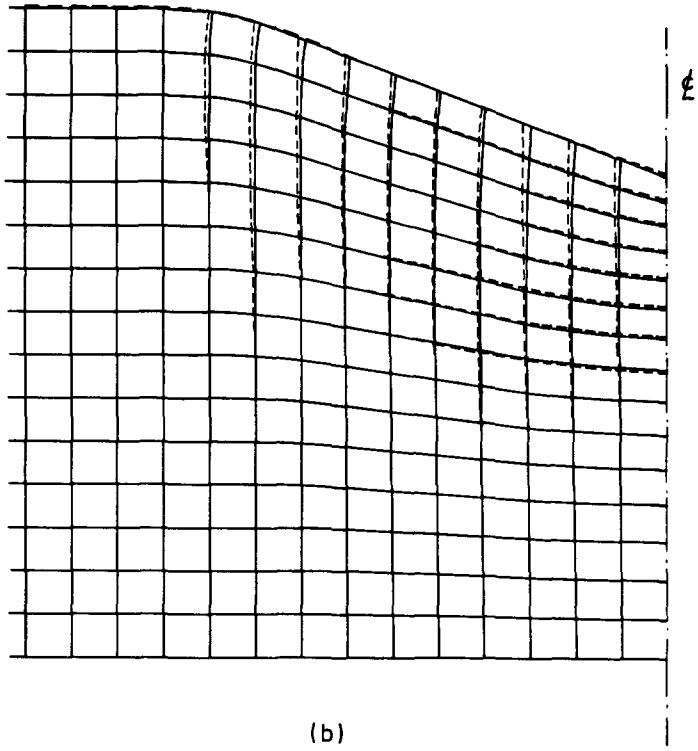

Fig. 18. (a) Deformed grid in indentation test, due to an indent of depth 2 mm. (b) Comparison of deformation field predicted by finite element analysis (solid lines) with the observed deformation field (dotted lines). Interpolation of the actual deformed grid is used in order for the two sets of grids to possess the same spacing.

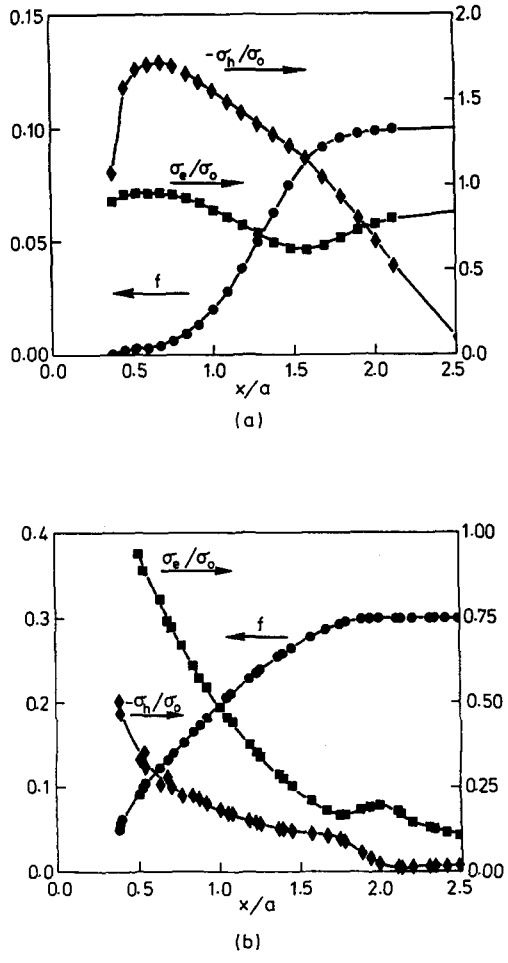

Fig. 16. Variation of normalized macroscopic effective stress, σ_e/σ_0, normalized hydrostatic stress, σ_h/σ_0, and porosity, f, directly ahead of indenter along the axis of symmetry. (a) Gurson solid, with initial porosity $f_0 = 0.1$, (b) FKM solid, with initial porosity $f_0 = 0.3$. $E_0/\sigma_0 = 500$, $\nu_0 = 0.3$, $\beta = 19.7°$.

$f_0 = 0.257$ and the dimensions given in Fig. 17 were employed. Uniaxial compression tests were performed in order to measure the material parameters. The measured elastic properties were $E = 64$ GPa and $\nu = 0.1$. Using $E_0 = 210$ GPa and $\nu_0 = 0.3$ as representative values for steels, together with $f = f_0 = 0.257$, in the linear relation (1) gives $E = 60$ GPa and $\nu = 0.086$. Based on a comparison of the measured uniaxial compressive response with the predictions of the FKM model, we used $\sigma_0 = 400$ MPa, and $N = 0.01$. With these parameters, the stress level was predicted within 10% up to a strain of 0.3, but the shape of the measured curve was not as concave as predicted by the FKM solid.

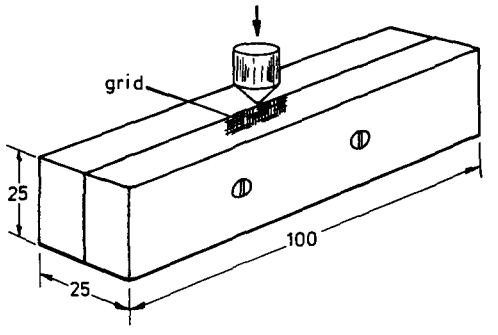

Fig. 17. Geometry of indentation test for sintered steel. All dimensions are in millimetres.

The indentation test was performed as follows. Two sintered steel bars were screwed together, and a hardened steel conical indenter of angle $\beta = 22°$ was aligned with the mating faces of the bars as shown in Fig. 17. Prior to testing the mating faces of the bars were polished and a square grid of 0.5 mm spacing was scribed onto one of the mating faces. The indentation was performed at a speed of 2×10^{-3} mm s^{-1} and to a penetration of 2 mm, using a screw driven test machine. After the test, the two bars were separated and the deformed grid was photographed, see Fig. 18a.

A finite element simulation of the indentation test was performed, for the case of the FKM constitutive law. Both the measured and the predicted load versus penetration responses were quadratic in shape, as demanded by the self-similarity of the problem. The two responses were in good agreement: at an indentation depth of 2 mm, the measured load was 33.0 kN and the predicted load was 32.6 kN.

The deformed finite element mesh and deformed grid are superimposed in Fig. 18b. Again, very good agreement is noted.

Acknowledgements—The authors are grateful for funding from the Nuffield Foundation and for the support provided by the Brown University Materials Research Group on the Micromechanics of Failure Resistant Materials, funded by the National Science Foundation. The authors wish to thank GKN Group Technology Ltd, Wolverhampton for provision of the test-pieces, and Mr A. K. Akisanya for experimental assistance. Computations reported here were carried out on the Cray YMP at the Pittsburgh Supercomputer Center and on an IBM RS/6000 workstation. We are indebted to Professor K. L. Johnson of Cambridge University and Dr A. F. Bower of Brown University for helpful comments.

REFERENCES

Bhattacharya, A. K. and Nix, W. D. (1988). Finite element simulation of indentation experiments. *Int. J. Solids Structures* **24,** 881–891.

Calladine, C. R. (1971). A microstructural view of the mechanical properties of saturated clay. *Géotechnique* **21,** 391–415.

Fleck, N. A., Kuhn, L. T. and McMeeking, R. M. (1992). Yielding of metal powder bonded by isolated contacts. *J. Mech. Phys. Solids* (in press).

Gibson, L. J. and Ashby, M. F. (1988). *Cellular Solids: Structure and Properties*. Pergamon Press, Oxford.

Green, A. P. (1954). The plastic yielding of metal junctions due to combined shear and pressure. *J. Mech. Phys. Solids* **2,** 197–211.

Gurson, A. L. (1975). Plastic flow and fracture behavior of ductile materials incorporating void nucleation, growth and interaction. Ph.D. Thesis, Brown University.

Gurson, A. L. (1977). Continuum theory of ductile rupture by void nucleation and growth: part 1—yield criteria and flow rules for porous ductile media. *J. Engng Mater. Tech.* **99,** 2–15.

Helle, A. S., Esterling, K. E. and Ashby, M. F. (1985). Hot isostatic pressing diagrams: new developments. *Acta Metall.* **33,** 2163–2174.

Hill, R. (1950). *The Mathematical Theory of Plasticity*. Clarendon Press, Oxford.

Johnson, K. L. (1970). The correlation of indentation experiments. *J. Mech. Phys. Solids* **18,** 115–126.

Johnson, K. L. (1985). *Contact Mechanics*. Cambridge University Press, Cambridge.

Koplik, J. and Needleman, A. (1988). Void growth and coalescence in porous plastic solids. *Int. J. Solids Structures* **24,** 835–853.

Lemaitre, J. (1985). A continuous damage mechanics model for ductile fracture. *J. Engng Mater. Tech.* **107,** 83–89.

Marsh, D. M. (1964). Plastic flow in glass. *Proc. R. Soc. London* **A279,** 420–435.

Needleman, A. (1982). Finite elements for finite strain plasticity problems. In *Plasticity of Metals at Finite Strain: Theory, Computation and Experiment* (Edited by E. H. Lee and R. L. Mallett), pp. 387–436. RPI, Troy, New York.

Peirce, D., Shih, F. and Needleman, A. (1984). A tangent modulus method for rate dependent solids. *Comput. Struct.* **18,** 875–887.

Rice, R. W. (1977). Microstructural dependence of mechanical behavior of ceramics. In *Treatise on Materials Science and Technology* (Edited by R. K. MacCrone), Vol. 11, pp. 200–381. Academic Press, New York.

Salak, A., Miskovic, V., Dudrova, E. and Rudnayova, E. (1974). The dependence of mechanical properties of sintered iron compacts upon density. *Powder Metall. Int.* **6,** 128–132.

Tabor, D. (1959). Junction growth in metallic friction: the role of combined stresses and surface contamination. *Proc. R. Soc. London* **A251,** 378–393.

Talmage, R. (1961). A new look at hardness–strength relationships in sintered metals. In *Progress in Power Metallurgy*, Vol. 17, pp. 168–175. Metal Powder Industry Federation, New York.

Timoshenko, S. P. and Goodier, J. N. (1970). *Theory of Elasticity* (3rd Edn). McGraw-Hill, New York.

Tvergaard, V. (1981). Influence of voids on shear band instabilities under plane strain conditions. *Int. J. Fract.* **17,** 389–407.

Wilsea, M., Johnson, K. L. and Ashby, M. F. (1975). Indentation of foamed plastics. *Int. J. Mech. Sci.* **17,** 457–461.